High Entropy Alloys & Materials
https://doi.org/10.1007/s44210-022-00010-8

ORIGINAL PAPER

Exceptional Soft Magnetic Properties of an Ordered Multi-principal Element Alloy with Disordered Nanoprecipitates

Youxiong Ye[1] · Scott D. Lish[1] · Liubin Xu[2] · Eric Woods[3] · Si Chen[4] · Yang Ren[4,6] · Markus W. Wittmann[1] · Haixuan Xu[2] · Baptiste Gault[3,5] · Ian Baker[1]

Received: 23 September 2022 / Accepted: 8 December 2022
© The Author(s), under exclusive licence to Springer Science+Business Media, LLC 2022

Abstract
In this work, a new non-equiatomic multi-principal element alloy (MPEA) $Fe_{40}Co_{30}Mn_{15}Al_{15}$ with excellent soft magnetic performance was fabricated. The microstructure and magnetic behavior of the as-cast alloy were investigated experimentally and theoretically using synchrotron X-ray diffraction, transmission electron microscopy, atom probe tomography, vibrating sample magnetometry, and density functional theory calculations. The alloy consists of an ordered B2-phase matrix enriched with Co/Al and uniformly distributed BCC nanoprecipitates enriched with Fe/Mn. The new alloy exhibits a high saturation magnetization of ~ 158 Am^2/kg, a low coercivity of ~ 108 A/m, a high electrical resistivity of ~ 238 μΩ cm, and a high Curie temperature of ~ 1020 K, which shows an excellent combination of soft magnetic properties compared to previously reported MPEAs and conventional FeCo alloys. The findings thus provide a new perspective for designing high-performance materials for soft magnetic applications.

Keywords Multi-principal element alloy · Nanoprecipitates · Soft magnetic properties · Density functional theory

Introduction

Multi-principal element alloys (MPEAs), often referred to as high entropy alloys (HEAs), are a new class of alloys with multiple equiatomic or near-equiatomic mixing of metallic elements [1, 2]. In contrast to the traditional development of new alloys based on one major element, this multicomponent approach has expanded the compositional space of alloy design and attracted significant research interest. MPEAs are usually single-phase solid solutions, e.g., face-centered cubic (FCC) or body-centered cubic (BCC), or dual-phase structures produced through the precipitation of ordered compounds (such as FCC/$L1_2$ or BCC/B2) developed by tuning alloy compositions and/or thermomechanical processing [3–10]. These MPEAs have demonstrated some unusual mechanical properties, such as excellent combination of strength and ductility [7–9], good resistance to high-temperature softening [10] and fracture [4], and attractive tribological properties [11].

Soft magnetic materials are key to efficient power conversion with wide range of applications including wide-bandgap semiconductors, electric vehicles, and aerospace industries [12, 13]. As the world transitions to a more electrified vehicles with sustainable sources of energy, there has been an increasing demand for novel soft magnetic materials which enable improved efficiency of power transformation with less energy losses. Ideal soft magnetic materials for these applications have a high saturation magnetization (M_s), low coercivity (H_c), and high electrical resistivity (ρ). The aforementioned MPEAs offer a new perspective for the design of advanced soft magnetic materials and the soft magnetic performance of several MPEAs have been reported [14–26].

✉ Ian Baker
Ian.Baker@dartmouth.edu

1 Thayer School of Engineering, Dartmouth College, Hanover, NH 03755, USA

2 Department of Materials Science and Engineering, The University of Tennessee, Knoxville, TN 37996, USA

3 Max-Planck-Institut Für Eisenforschung, Max-Planck-Straße 1, 40237 Düsseldorf, Germany

4 X-Ray Science Division, Argonne National Laboratory, Lemont, IL 60439, USA

5 Department of Materials, Royal School of Mines, Imperial College London, Prince Consort Road, London SW7 2BP, UK

6 Present Address: Department of Physics, City University of Hong Kong, Kowloon, Hong Kong, China

Published online: 27 December 2022

Zhang et al. investigated a series of $FeCoNi(AlSi)_x$ MPEAs with various soft magnetic properties attained by adjusting the Al and Si content with the optimum balance of magnetic and electrical properties (M_s = 1.15 T or ~ 131 Am^2/kg, H_c = 1400 A/m, and ρ = 69.5 μΩ cm) being achieved for the FCC MPEA $FeCoNiAl_{0.2}Si_{0.2}$ [21]. They further studied another $(Fe_{0.3}Co_{0.5}Ni_{0.2})_{100-x}(Al_{1/3}Si_{2/3})_x$ alloy system and successfully optimized the soft magnetic properties with relatively high M_s close to 150 Am^2/kg and low H_c of 96 A/m for $(Fe_{0.3}Co_{0.5}Ni_{0.2})_{95}(Al_{1/3}Si_{2/3})_5$ alloy prepared via the maglev melting method [26]. It was recently reported that an excellent combination of a low coercivity of 78 A/m, a moderate saturation magnetization of 100 Am^2/kg, and good electrical resistivity of 103 μΩ cm was obtained via designing a FeCo–Ni–Ta–Al multicomponent alloy with ferromagnetic FCC matrix and paramagnetic coherent ordered FCC ($L1_2$) nanoparticles [3]. Jung et al. examined the effects of varying the Fe and Co content on the phase formation and soft magnetic behavior of $Al_{0.1}(Fe_{1+x}CoCr_{1-x}Mn)_{0.9}$ MPEAs and found that the MPEA $Al_{0.1}(Fe_{1.6}CoCr_{0.4}Mn)_{0.9}$, consisting of a disordered BCC matrix and nanoscale ordered BCC (B2) precipitates, showed the highest M_s of 135 Am^2/kg [27].

In this study, we designed an MPEA $Fe_{40}Co_{30}Mn_{15}Al_{15}$ with a B2 matrix containing disordered BCC nanoprecipitates. The microstructure, magnetic properties, and electrical resistivity of the alloy were investigated both experimentally and theoretically. The MPEA has an outstanding combination of soft magnetic and electrical performance, and is, thus, promising for advanced soft magnetic applications where high power density and low hysteresis-related and eddy-current-related energy losses are required.

Method

Experimental Procedure

An MPEA with a nominal composition of $Fe_{40}Co_{30}Mn_{15}Al_{15}$ (at.%) was prepared by arc melting a mixture of the constituent metals (99.97% Fe, 99.5% Co, 99.9% Mn, and 99.9% Al) in a Centorr Series 5 Bell Jar with a water-chilled copper crucible and a 2% lanthanated tungsten stinger under a Ti-gettered high-purity argon atmosphere. The ingot was flipped and remelted three times to ensure chemical homogeneity.

Synchrotron high-energy X-ray diffraction (XRD) of the as-cast alloy was conducted to investigate the crystal structure phases using beamline 11-ID-C (X-ray wavelength = 0.1173 Å) at the Advanced Photon Source at Argonne National Laboratory. A Thermo Fisher Tecnai F20 field emission gun (FEG) transmission electron microscope (TEM) was utilized for microstructural characterization of the alloy at an accelerating voltage of 200 kV. Specimens for TEM observations were prepared by mechanically grinding and polishing 3-mm-disk samples and then further thinning via twin-jet electropolishing in a Struers TenuPol-5 unit with a solution of 15 v/v% nitric acid in methanol at ~ 14 V at a temperature of 253 K. Atom probe tomography (APT) was undertaken to analyze the local chemical compositions of different phases by employing a local electrode atom probe (LEAP), 5000 XR (Cameca Instrument Inc., Madison, WI, USA). Laser-assisted field evaporation was performed at 50 K by applying a laser pulse energy of 40 pJ at a repetition rate of 125 kHz. Samples for APT were prepared from a bulk sample using a Helios Plasma FIB/SEM (FEI, Hillsboro, OR, USA) and placed onto a standard 36-post APT coupon (Cameca Instruments, Inc., Madison, WI, USA).

Cube-shaped specimens with dimensions of ~ 2.3 mm × 2.3 mm × 2.3 mm were used for magnetic properties measurements on a Lakeshore Instruments 7300 vibrating sample magnetometer (VSM). Magnetic hysteresis loops were performed at room temperature under a maximum applied field of 10 kOe (or ~ 800 kA/m) with at least three tests to obtain M_s and H_c. The Curie temperature, T_c, was also measured with the VSM from 323 to 1223 K under an applied field of 5 kOe (or ~ 400 kA/m). The electrical resistivity ρ was measured on sheet specimens with thicknesses of ~ 0.5 mm using a Four-Point Probe Resistivity system. The reported values are the average of ten measurements.

Computational Methodology

Density functional theory (DFT) simulations were employed to investigate the magnetic structures of the B2 and BCC phases in the MPEA. The simulations were performed using the Vienna Ab Initio Simulation Package (VASP) [28, 29], in which the projector-augmented wave method was adopted [30]. The Perdew–Burke–Ernzerhof (PBE) functional [31] was chosen as the exchange–correlation functional while the plane wave energy cut-off was set as 405 eV. Three 4 × 4 × 4 cubic supercells of different atomic arrangements were constructed to represent the B2 matrix and the BCC precipitate, respectively (examples shown in Fig. 5a and 5b). The special quasi-random structure (SQS) technique [32], as implemented in the Alloy Theoretic Automated Toolkit [33, 34], was applied to improve the representativeness of the alloy configuration sampling, with up to third nearest neighbors considered for the pair correlations and first for the triplet. BCC and B2 structured supercells with compositions corresponding to the values measured by APT were used for the DFT calculations (Table 1). The atomic configuration in the sub-lattice of the B2 phase was constructed by assuming that it is similar to a B2 structured $Fe_{30}Co_{40}Al_{15}Mn_{15}$ alloy in our previous study [16] in which the atomic site occupancy

Table 1 Chemical compositions (at.%) of $Fe_{40}Co_{30}Mn_{15}Al_{15}$ obtained from APT analyses

	Fe	Co	Mn	Al
Overall	38.0 ± 0.1	30.4 ± 0.1	14.9 ± 0.1	16.6 ± 0.1
BCC precipitates	50.1 ± 1.8	12.2 ± 1.8	28.9 ± 2.3	8.8 ± 1.1
B2 matrix	36.2 ± 0.1	32.4 ± 0.1	13.7 ± 0.1	17.7 ± 0.1

was determined using a TEM/EDS-based technique, i.e., ALCHEMI (Atom Location by CHanneling Enhanced MIcroanalysis) [35]. For the structure optimization, two strategies were employed: in the first strategy we allowed only the ionic movements and fixed the lattice parameters as the experimental ones, while in the second strategy we optimized both the ionic positions and the lattice parameters. The first strategy reflected the relative strain conditions between the matrix and the precipitate as observed in the experiments, while the second would eliminate the influence of possibly excessive strain due to the discrepancy between the DFT and the experimental lattice parameters. The force criterion was 0.01 eV/ Å and the electronic convergence criterion was 10^{-6} eV. The 2 × 2 × 2 gamma-centered Monkhorst–Pack k-point grid was used in the structural optimization, while the 4 × 4 × 4 grid of the same scheme was used in the density of state (DOS) calculation. Regarding the initial magnetic structures, collinear magnetism description was adopted. The Fe, Co, and Al atoms were set to have parallel moments, whereas four cases were considered for the moments of Mn, i.e., Mn moments parallel to the rest, Mn moments antiparallel, and Mn on one sublattices parallel, while those on the other sublattices antiparallel.

Results

Figure 1a shows a synchrotron XRD pattern of the as-cast $Fe_{40}Co_{30}Mn_{15}Al_{15}$ alloy. The diffraction pattern shows peaks associated with B2 ordered structure, indicating that the current alloy could be either single B2 phase or a mixture of both B2 and disordered BCC phases. Dark-field (DF) TEM images of the as-cast specimen viewed along [110] and [100] are shown in Fig. 2a and c. The presence of {001} superlattice reflections in their corresponding selected area diffraction patterns (SAED), in Fig. 2b and d, confirms the B2 ordering. The DF images obtained under $\boldsymbol{g} = 001$ and $\boldsymbol{g} = 010$ superlattice reflections clearly reveal an ordered B2 matrix with bright contrast and disordered BCC precipitates with dark contrast. These rod-like, BCC nanoscale precipitates, which are ~ 9 nm wide and ~ 22 nm long, are uniformly distributed in the B2 matrix. The lattice parameters determined from synchrotron XRD (Fig. 1b) are 2.8780 ± 0.0016 Å and 2.8770 ± 0.0010 Å for the BCC and B2 phases, respectively.

In order to quantitatively analyze the elemental partitioning between the two B2/BCC phases, 3D-APT analysis was performed. The elemental maps and iso-concentration surface of 20 at.% Mn are displayed in Fig. 3a, highlighting the disordered BCC precipitates. The results show an inhomogeneous elemental distributions with Fe and Mn enrichments in the precipitates. A typical compositional profile

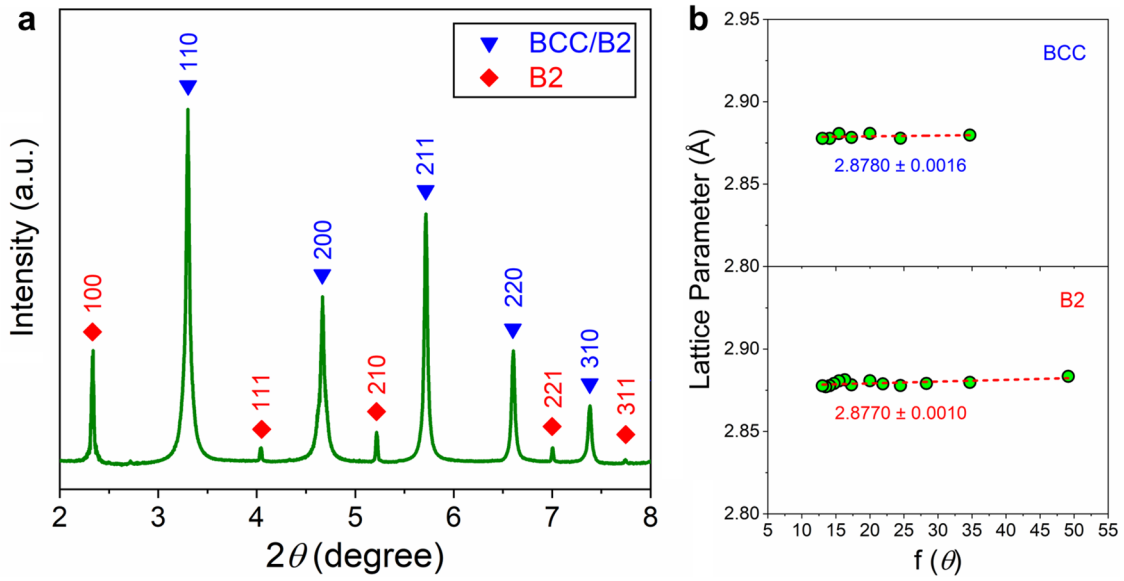

Fig. 1 **a** Synchrotron XRD pattern of $Fe_{40}Co_{30}Mn_{15}Al_{15}$ alloy. **b** Plots of measured lattice parameter values versus $f(\theta)$ of each peak for BCC and B2 phases, where $f(\theta) = \cos^2(\theta) \cdot (1/\sin\theta + 1/\theta)/2$ and θ is the Bragg angle of each peak. The best lattice parameters (a) were obtained at $f(\theta) = 0$ (i.e., y-intercept) [36]

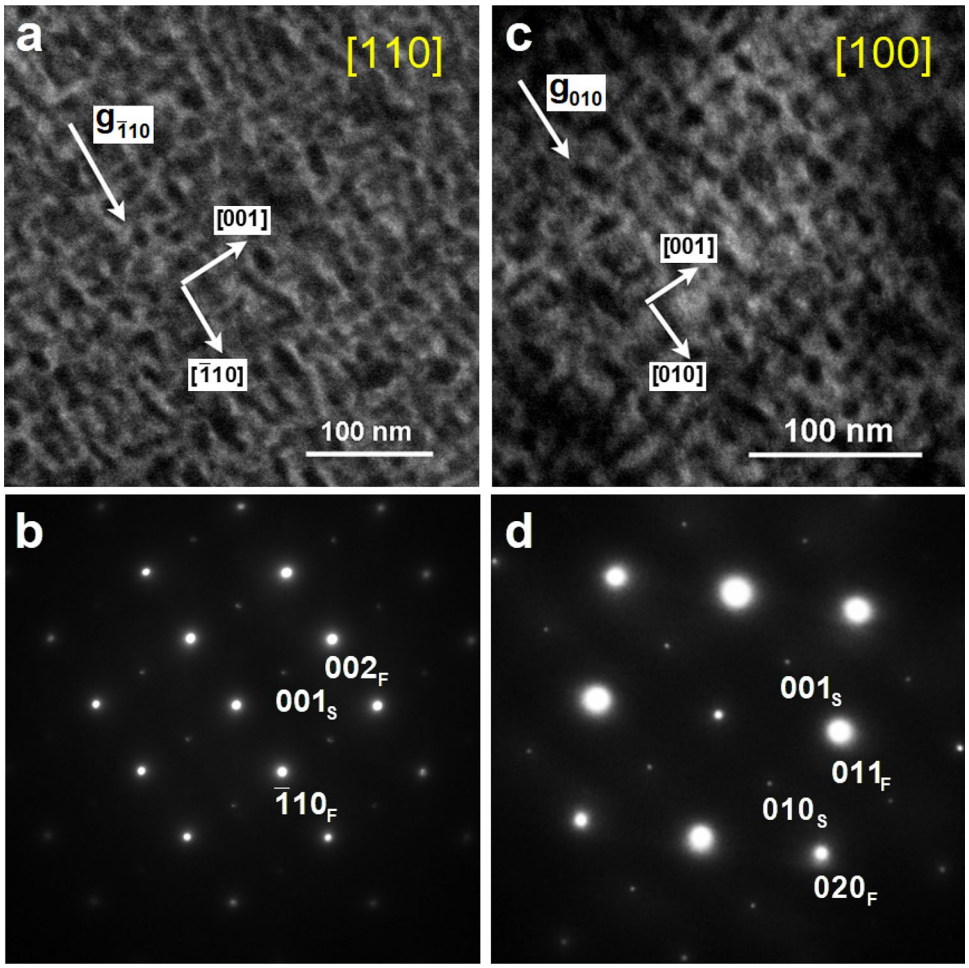

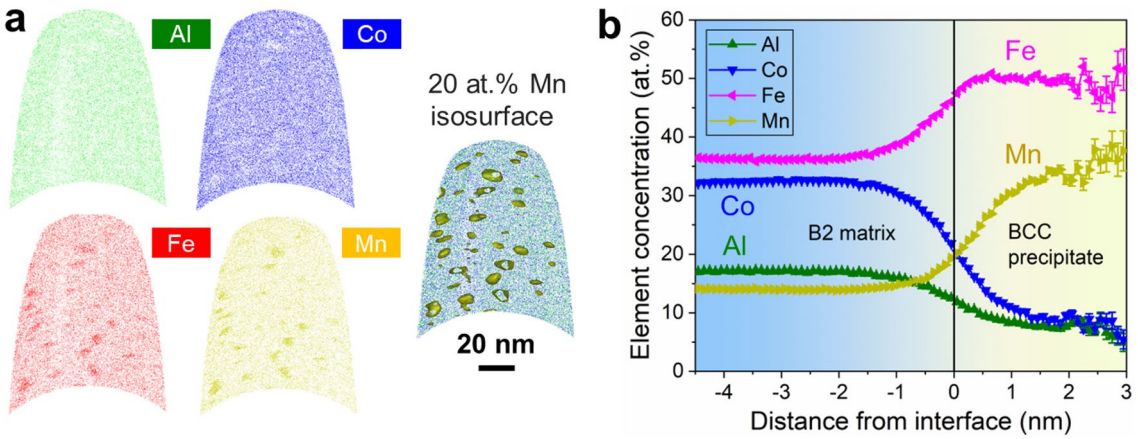

Fig. 2 Dark-field (DF) TEM images and the corresponding SAED patterns of $Fe_{40}Co_{30}Mn_{15}Al_{15}$ alloy along (**a**, **b**) [110] zone and **c**, **d** [100] zone axes. The diffraction vectors ***g*** used to obtain the images are indicated. In the SAED patterns, "F" indicates fundamental reflections and "S" indicates superlattice reflections

Fig. 3 **a** APT reconstructions of principal elements and iso-concentration surface of 20 at.% Mn from the analysis of $Fe_{40}Co_{30}Mn_{15}Al_{15}$ alloy. **b** Elemental concentration profiles across the interface between the B2 matrix and BCC precipitate

across the B2/BCC interface is shown in Fig. 3b. It is readily observed that the Fe and Mn partition to the disordered BCC precipitates, whereas the Co and Al partition to the B2 matrix. Specifically, the BCC phase contains ~ 50 at.% Fe and ~ 29 at.% Mn while the B2 phase contains ~ 36 at.% Co and ~ 18 at.% Al, see Table 1. The stoichiometries of the BCC nanoprecipitates and B2 matrix were determined to be $Fe_{50}Co_{12}Mn_{29}Al_9$ and $Fe_{36}Co_{32}Mn_{14}Al_{18}$ (at.%), respectively.

The elemental partitioning can be further quantified in terms of partitioning coefficient (K_i), defined as the ratio of the concentration of element i in the B2 (C_i^{B2}) to the concentration of the same element in the BCC phase (C_i^{BCC}) [37]:

$$K_i = C_i^{B2}/C_i^{BCC} \tag{1}$$

The partitioning coefficient is calculated to be 0.7, 2.7, 0.5, 2.0 for Fe, Co, Mn, Al, respectively. For K_i values in excess of 1, the Co exhibits a slightly higher preferential partitioning to the B2 matrix than the Al. Conversely, as indicated by the K_i values less than unity, somewhat larger segregation of Mn in the BCC phase than that of Fe can be inferred. Meanwhile, volume fractions of B2 and BCC phases can be calculated based on the lever rule for two-phase alloys [37]:

$$C_i^{bulk}=C_i^{B2} \cdot V_{B2} + C_i^{BCC}(1 - V_{B2}), \tag{2}$$

where V_{B2} is the volume fraction of B2 matrix and C_i^{bulk} is the overall concentration of i element in the alloy. The volume fraction of B2 matrix can be rewritten as

$$V_{B2}=(C_i^{bulk} - C_i^{BCC})/(C_i^{B2} - C_i^{BCC}). \tag{3}$$

Therefore, the phase volume fractions for B2 matrix and BCC nanoprecipitates are calculated as 89.7% and 10.3%, respectively.

A representative magnetic hysteresis loop for the $Fe_{40}Co_{30}Mn_{15}Al_{15}$ alloy acquired using the VSM is shown in Fig. 4a. It is readily seen that the MPEA can be easily magnetized to the saturated state and exhibits a low H_c when demagnetized. Specifically, an excellent combination of high M_s of 157.7 Am^2/kg and low H_c of 107.8 A/m indicates its potential as a soft magnetic material (H_c < 1000 A/m). Interestingly, although the alloy shows a mixture of B2 matrix and BCC precipitates, a low coercivity can still be obtained. It has been shown that the coercivity scales with particle size with a theoretical relationship of $H_c \propto D_p^{\,6}$ when the particles are in nanoscale range [23, 38]. Therefore, these nanoscale precipitates have a relatively small pinning effect on domain wall movement within the material, resulting in the low coercivity. The temperature dependence of M_s of the alloy is shown in Fig. 4b. As the temperature increases, the M_s gradually decreases to ~ 100 Am^2/kg at 800 K, followed by a sharp drop to near zero at > 1050 K. The Curie temperature T_c was determined to be ~ 1020 K, suggesting its potential use at high temperatures. The relatively small change of M_s at lower temperatures is associated with the fact that the thermal vibration of atoms does not substantially affect the magnetic ordering when the temperature is far below T_c [15]. Additionally, the alloy exhibits a high electrical resistivity of 238 ± 8 μΩ cm, suggesting a low eddy current loss. Further comparisons of soft magnetic performance with other reported soft magnets will be discussed.

We also performed density functional theory (DFT) calculations to understand the magnetic behavior of the $Fe_{40}Co_{30}Mn_{15}Al_{15}$ alloy, as shown in Fig. 5. The compositions of the B2 matrix and BCC precipitates measured by APT (Table 1) were used to construct the respective supercells (Fig. 5a, b) during the DFT calculations. The magnetic contributions of each element were analyzed via the total density of states (DOS), partial DOS (pDOS), and elemental magnetic moment. The total DOS of both the B2 matrix and

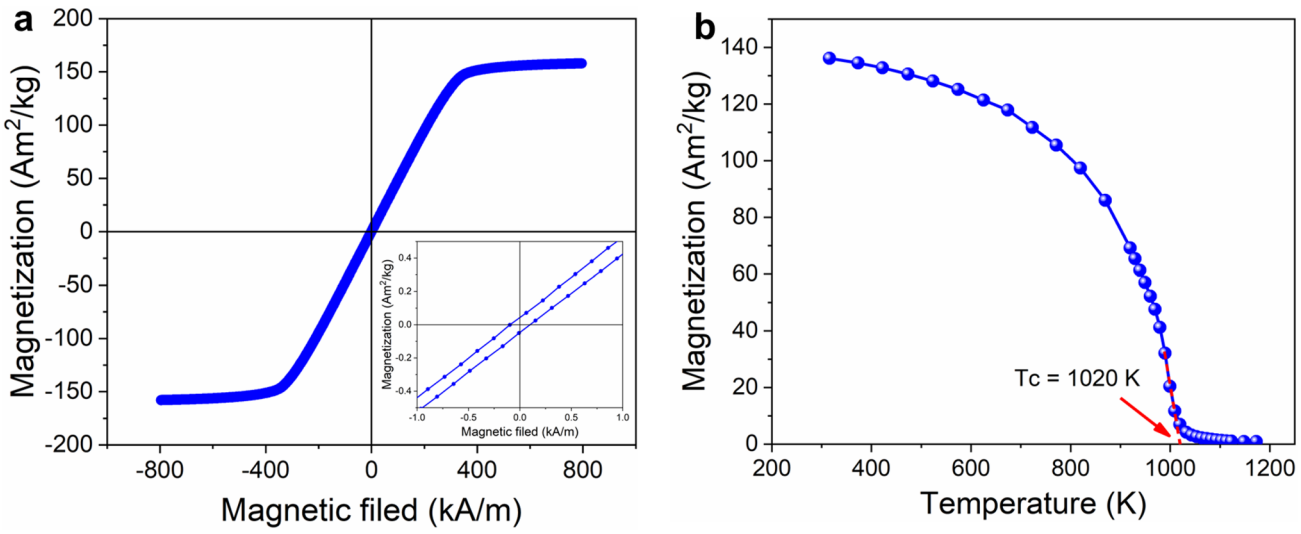

Fig. 4 **a** Representative magnetic hysteresis loop of $Fe_{40}Co_{30}Mn_{15}Al_{15}$ alloy. The inset shows an enlarged view of the loop at low magnetic fields. **b** Temperature dependence of the magnetization of $Fe_{40}Co_{30}Mn_{15}Al_{15}$ alloy at an applied magnetic field of 400 kA/m

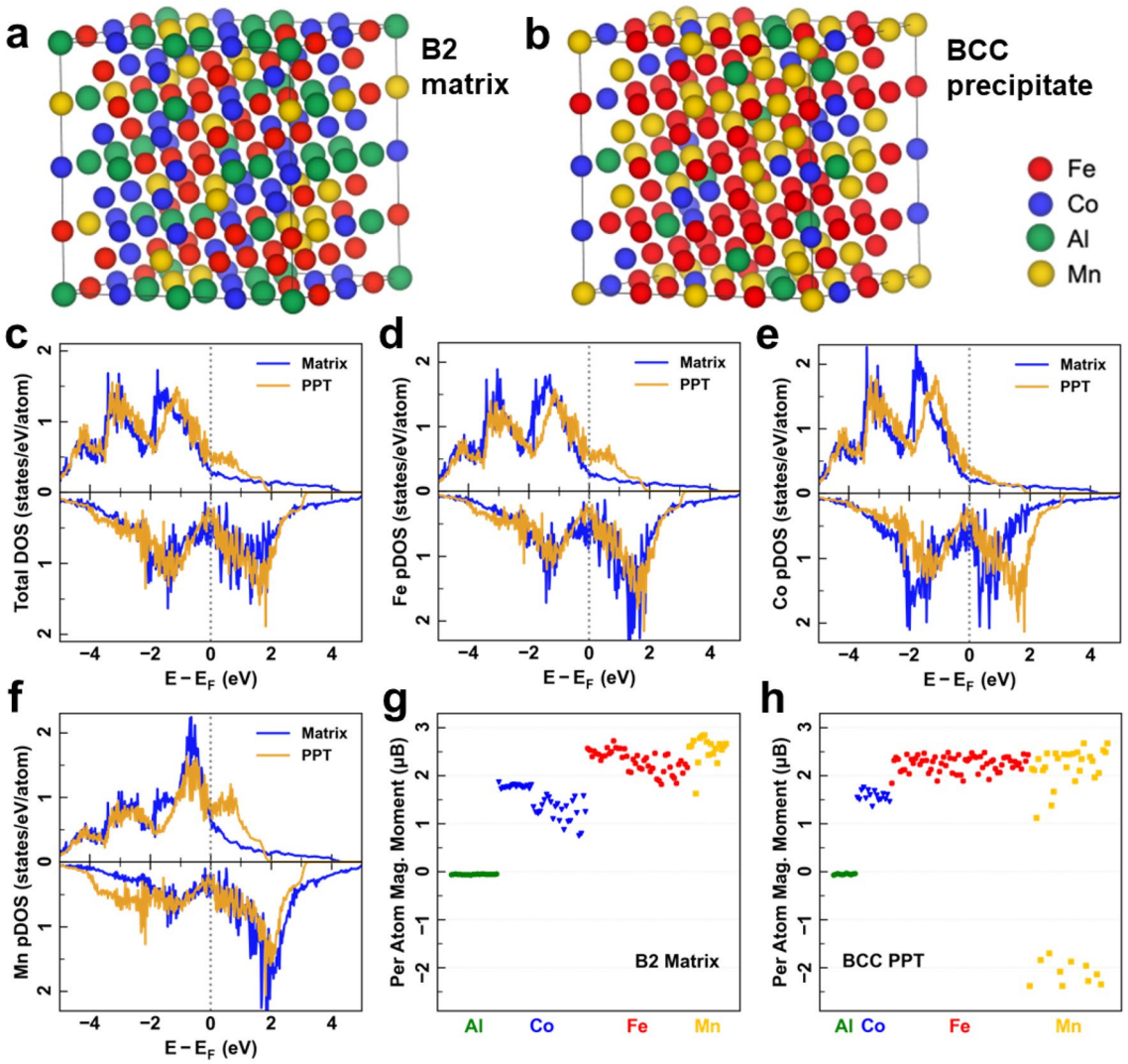

Fig. 5 Atomistic configurations of the **a** B2 matrix and **b** BCC precipitate phases. **c** Total, **d** Fe, **e** Co, and **f** Mn density of states (DOS) of B2 and BCC phases. Calculated elemental magnetic moments for the **h** B2 matrix and **i** BCC precipitate phases

the BCC precipitates exhibit typical ferromagnetic profile (Fig. 5c). They are similar to the pDOS of the two major elements, i.e., Fe (Fig. 5d) and Co (Fig. 5e), which can be reasoned through the rigid band model [39]. The Mn pDOS (Fig. 5f) in the matrix shows smaller difference between the spin-up and spin-down components in comparison with the precipitates, which can be associated with the reduced Al concentration in the BCC precipitates as the presence of Al can reduce the exchange splitting [14, 27]. The pDOS plots are further corroborated by the per-atom magnetic moments shown in Fig. 5g and 5h, where all Fe and Co moments were ferromagnetically coupled for both phases, while the Mn atoms displayed ferromagnetic coupling in the B2 matrix but high variance in the BCC precipitates. Further, it was found that the Mn atoms with negative moments exhibited more local Mn–Mn bonding up to the 2nd nearest neighbors. This is similar to the relationship between the Mn–Mn distance and the magnetic structure in the NiAs-type Mn compound [40]. According to Slater–Bethe curve [41–43], when the equivalent Mn–Mn distance is lowered due to increased Mn concentration, direct exchange coupling between the Mn pairs is enhanced, inducing the antiferromagnetic coupling because of Mn's half-filled *d* bands.

We also estimated the theoretical M_s of the material, including both B2 matrix and BCC precipitate phases, via their atomic magnetic moments [27]:

$$M_{s,phase} = \frac{\mu_{B,\ supercell}}{W_{supercell}}, \tag{4}$$

where $M_{s,\ phase}$ is the theoretical M_s, of each phase, $\mu_{B,\ supercell}$ is the total magnetic moment in either B2 or BCC supercells

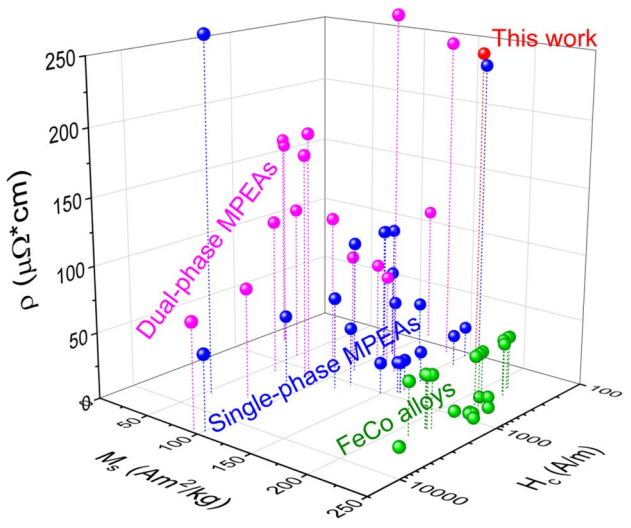

Fig. 6 3D plot compiling room-temperature M_s, H_c, and ρ for a variety of single-phase [16–21] and dual-phase [3, 19–23] MPEAs as well as conventional FeCo alloys [23, 44–48]

($\mu_B = 9.274 \times 10^{-24}$ Am^2 is the Bohr magneton), and $W_{\text{supercell}}$ is the total atomic weight of the supercells. The total $M_{s,\,total}$ value of the alloy can be estimated from a rule of mixture:

$$M_{s,total} = V_{B2}M_{s,B2} + V_{BCC}M_{s,BCC}, \quad (5)$$

where V_{B2} and V_{BCC} are the volume fractions of each phase as obtained from the APT analysis. The calculated M_s for the B2 matrix and the BCC precipitates are 177.6 Am^2/kg and 169.9 Am^2/kg, respectively. Interestingly, both phases show excellent ferromagnetism, i.e., the BCC precipitates do not compromise the magnetization of the material. As a result, the overall magnetization is thus estimated as 176.8 Am^2/kg, which agrees well with the experimentally determined value of 157.7 Am^2/kg. The slight overestimate may result from the fact that the DFT calculations were performed at 0 K, whereas the VSM measurements were conducted at room temperature.

To highlight the good combination of soft magnetic properties and electrical resistivity of the $Fe_{40}Co_{30}Mn_{15}Al_{15}$ MEPA, we compiled its room-temperature M_s, H_c, and ρ into a 3D plot, in Fig. 6, together with other existing MPEAs, including single-phase and dual-phase MEPAs, and conventional FeCo alloys in literature (summarized in Table 2). It is readily observed that the current alloy (shown as a red sphere) has an excellent combination of relatively high M_s (157.7 Am^2/kg), low H_c (107.8 A/m), and high ρ (238 μΩ cm), outperforming the most reported MPEAs as well as conventional FeCo alloys. The majority of single-phase MPEAs exhibit relatively low electrical resistivity and most dual-phase MPEAs display somewhat low saturation magnetization. Two recently developed MPEAs [16, 23] show the most comparable combinations to the currently alloy. The dual-phase B2/BCC $Al_{1.5}Co_4Fe_2Cr$ HEA (the pink sphere near the red sphere) shows a higher ρ, but a lower Ms and a higher H_c than for our alloy; and the single-phase B2 $Fe_{30}Co_{40}Mn_{15}Al_{15}$ MPEA (the blue sphere near the red sphere) shows a slightly higher M_s, but also a higher H_c and lower ρ than the current alloy. It is interesting that similar magnetic properties were obtained for the previous single-phase B2 $Fe_{30}Co_{40}Mn_{15}Al_{15}$ and the current dual-phase B2/BCC $Fe_{40}Co_{30}Mn_{15}Al_{15}$ alloys. Our DFT calculations (Fig. 5) indicate that the Fe/Mn-rich BCC precipitates show good ferromagnetism, i.e., the ferromagnetic BCC precipitates would essentially not impair the magnetization. On the other hand, relatively small pinning effect on domain wall movement leads to low coercivity due to their very fine sizes of nanoprecipitates [23, 38]. Although the M_s of the current $Fe_{40}Co_{30}Mn_{15}Al_{15}$ MEPA is not comparable to that of conventional FeCo alloys, its exhibits lower H_c yet much higher ρ, allowing lower energy losses from hysteresis and eddy current losses. Furthermore, the new $Fe_{40}Co_{30}Mn_{15}Al_{15}$ alloy also enables a reduction in the cost in comparison with the conventional FeCo alloys (e.g., commercial FeCo–2V) due to the lower content or replacement of the high-cost elements Co and/or V via substantially alloying with the inexpensive Mn and Al.

Conclusions

In summary, we have developed a new non-equiatomic $Fe_{40}Co_{30}Mn_{15}Al_{15}$ MPEA and investigated its microstructure and soft magnetic properties experimentally and theoretically. The alloy consists of an ordered B2 matrix and nanoscale BCC precipitates with Co and Al elements partitioning to the former phase and Fe and Mn elements partitioning to the latter phase. This alloy unifies excellent soft magnetic properties and electrical resistivity with a high saturation magnetization of ~ 158 Am^2/kg, a low coercivity of ~ 108 A/m, a high electrical resistivity of ~ 238 μΩ cm, and a high Curie temperature of ~ 1020 K, which outperforms most reported MPEAs and traditional FeCo alloys in the literature. DFT calculations revealed that both B2 matrix and BCC nanoprecipitates are highly ferromagnetic and their overall magnetization agrees well with experimental results. Our current study offers a new alloy design strategy for developing high-performance soft magnetic alloys via ferromagnetic multicomponent B2 matrix and BCC nanoprecipitates.

Table 2 Alloy composition (at.%), crystal structures, saturation magnetization (M_s), coercivity (H_c), and electrical resistivity (ρ) of a variety of soft magnetic MPEAs. Conventional FeCo and FeCo–2V alloys are also included for comparison

Alloys	Structure	M_s (Am^2/kg)	H_c (A/m)	ρ (μΩ cm)	References
FeCo	B2	210–230[a]	435–4615	1.95	[44–47]
FeCo–2V	B2	212–219[a]	240–2900	40–46.4	[23, 47, 48]
FeCoNi	FCC	150–160	121–1069	16.7–24	[17, 19–21]
$FeCoNi(AlSi)_{0.1}$	FCC	122.0[a]	1089	44.4	[21]
$FeCoNi(AlSi)_{0.2}$	FCC	116.7[a]	1400	69.5	[21]
$FeCoNi(AlSi)_{0.4}$	BCC	102.4[a]	17,963	57.3	[21]
$FeCoNi(AlSi)_{0.5}$	BCC	82.5[a]	1937	52.0	[21]
$FeCoNi(AlSi)_{0.8}$	BCC	56.7[a]	5952	264.0	[21]
$FeCoNiAl_{0.25}$	FCC	130	230.8	46.2	[20]
FeCoNiAl	BCC	101.8	222.8	65	[20]
$FeCoNiSi_{0.25}$	FCC	126	397.9	53	[20]
$FeCoNi(MnAl)_{0.25}$	FCC	101–104	268–629	91–110	[18, 19]
$Fe_{30}Co_{40}Mn_{15}Al_{15}$	B2	162.4	113.6	230	[16]
$FeCoNi(AlSi)_{0.3}$	FCC + BCC	95.0[a]	19,336	79.7	[21]
$FeCoNiAl_{0.5}$	FCC + BCC	105	358.1	77	[20]
$FeCoNiAl_{0.75}$	FCC + BCC	110	318.3	67.1	[20]
$FeCoNiSi_{0.5}$	FCC + Ni_3Si	91.5	477.5	84	[20]
$FeCoNiSi_{0.75}$	FCC + Ni_3Si	81	4535.9	83	[20]
$FeCoNi(MnAl)_{0.5}$	FCC + BCC	52–89	730–1565	118	[19]
$FeCoNi(MnAl)_{0.75}$	BCC + FCC	129.6	445	271	[19]
FeCoNiCrAl	BCC + B2	20–89	467–565	160–187	[22]
$Al_{1.5}Co_4Fe_2Cr$	B2 + BCC	135.3	127.3	244	[23]
FeCo–Ni–Ta–Al	FCC + $L1_2$	100	78	103	[3]
$Fe_{40}Co_{30}Mn_{15}Al_{15}$	B2 + BCC	157.7	107.8	238	This work

[a]The units for M_S for conventional FeCo-based alloys and $FeCoNi(AlSi)_x$ MPEAs were converted from Tesla via equation $B_S = 4\pi M_S \rho_m / 10^4$, in which rule of mixture were used for density (ρ_m) estimation for $FeCoNi(AlSi)_x$ MPEAs without available density data in the literature

Acknowledgements This work was supported by NIST grant 60NANB2D0120 and U.S. National Science Foundation Grant Number 1758924. L.X. and H.X. are supported by the National Science Foundation under Grant No. DMR-1654438. This work used the Extreme Science and Engineering Discovery Environment (XSEDE), which is supported by the National Science Foundation grant number TG-DMR17012. This research used resources of the Advanced Photon Source, a U.S. Department of Energy (DOE) Office of Science User Facility, operated for the DOE Office of Science by Argonne National Laboratory under Contract No. DE-AC02-06CH11357. The views and conclusions contained herein are those of the authors and should not be interpreted as necessarily representing official policies, either expressed or implied, of the National Science Foundation, or the U.S. Government.

Data Availability The datasets generated during and/or analyzed during the current study are available from the corresponding author on reasonable request.

Declarations

Conflict of interest The authors declare no conflict of interest.

References

1. J.W. Yeh, S.K. Chen, S.J. Lin, J.Y. Gan, T.S. Chin, T.T. Shun, C.H. Tsau, S.Y. Chang, Nanostructured high-entropy alloys with multiple principal elements: novel alloy design concepts and outcomes. Adv. Eng. Mater. **6**, 299–303 (2004)
2. B. Cantor, I.T.H. Chang, P. Knight, A.J.B. Vincent, Microstructural development in equiatomic multicomponent alloys. Mater. Sci. Eng. A **375**, 213–218 (2004)
3. L. Han, F. Maccari, I.R. SouzaFilho, N.J. Peter, Y. Wei, B. Gault, O. Gutfleisch, Z. Li, D. Raabe, A mechanically strong and ductile soft magnet with extremely low coercivity. Nature **608**, 310–316 (2022)
4. B. Gludovatz, A. Hohenwarter, D. Catoor, E.H. Chang, E.P. George, R.O. Ritchie, A fracture-resistant high-entropy alloy for cryogenic applications. Science **345**, 1153–1158 (2014)
5. Y. Ma, Q. Wang, B. Jiang, C. Li, J. Hao, X. Li, C. Dong, T. Nieh, Controlled formation of coherent cuboidal nanoprecipitates in body-centered cubic high-entropy alloys based on Al2 (Ni Co, Fe, Cr) 14 compositions. Acta Mater. **147**, 213–225 (2018)

6. Y.X. Ye, B. Ouyang, C.Z. Liu, G.J. Duscher, T.G. Nieh, Effect of interstitial oxygen and nitrogen on incipient plasticity of NbTiZrHf high-entropy alloys. Acta Mater. **199**, 413–424 (2020)
7. J.Y. He, H. Wang, H.L. Huang, X.D. Xu, M.W. Chen, Y. Wu, X.J. Liu, T.G. Nieh, K. An, Z.P. Lu, A precipitation-hardened high-entropy alloy with outstanding tensile properties. Acta Mater. **102**, 187–196 (2016)
8. Z. Lei, X. Liu, Y. Wu, H. Wang, S. Jiang, S. Wang, X. Hui, Y. Wu, B. Gault, P. Kontis, D. Raabe, L. Gu, Q. Zhang, H. Chen, H. Wang, J. Liu, K. An, Q. Zeng, T.-G. Nieh, Z. Lu, Enhanced strength and ductility in a high-entropy alloy via ordered oxygen complexes. Nature **563**, 546–550 (2018)
9. Z. Wang, I. Baker, Z. Cai, S. Chen, J.D. Poplawsky, W. Guo, The effect of interstitial carbon on the mechanical properties and dislocation substructure evolution in $Fe_{40.4}Ni_{11.3}Mn_{34.8}Al_{7.5}Cr_6$ high entropy alloys. Acta Mater. **120**, 228–239 (2016)
10. O.N. Senkov, G.B. Wilks, J.M. Scott, D.B. Miracle, Mechanical properties of $Nb_{25}Mo_{25}Ta_{25}W_{25}$ and $V_{20}Nb_{20}Mo_{20}Ta_{20}W_{20}$ refractory high entropy alloys. Intermetallics **19**, 698–706 (2011)
11. Y.X. Ye, C.Z. Liu, H. Wang, T.G. Nieh, Friction and wear behavior of a single-phase equiatomic TiZrHfNb high-entropy alloy studied using a nanoscratch technique. Acta Mater. **147**, 78–89 (2018)
12. J.M. Silveyra, E. Ferrara, D.L. Huber, T.C. Monson, Soft magnetic materials for a sustainable and electrified world. Science **362**, eaao0195 (2018)
13. V. Chaudhary, R. Chaudhary, R. Banerjee, R.V. Ramanujan, Accelerated and conventional development of magnetic high entropy alloys. Mater. Today **49**, 231–252 (2021)
14. T. Zuo, M.C. Gao, L. Ouyang, X. Yang, Y. Cheng, R. Feng, S. Chen, P.K. Liaw, J.A. Hawk, Y. Zhang, Tailoring magnetic behavior of CoFeMnNiX (X = Al, Cr, Ga, and Sn) high entropy alloys by metal doping. Acta Mater. **130**, 10–18 (2017)
15. T. Zuo, M. Zhang, P.K. Liaw, Y. Zhang, Novel high entropy alloys of $Fe_xCo_{1-x}NiMnGa$ with excellent soft magnetic properties. Intermetallics **100**, 1–8 (2018)
16. Youxiong Ye, Scott D. Lish, Liubin Xu, Si Chen, Yang Ren, Aparna Saksena, Baptiste Gault, Markus W. Wittmann, Haixuan Xu, I. Baker, $Fe_{30}Co_{40}Mn_{15}Al_{15}$: a Novel Single-Phase B2 Multi-Principal Component Alloy Soft Magnet, High Entropy Alloys & Materials, (2022).
17. M.S.K.K.Y. Nartu, A. Jagetia, V. Chaudhary, S.A. Mantri, E. Ivanov, N.B. Dahotre, R.V. Ramanujan, R. Banerjee, Magnetic and mechanical properties of an additively manufactured equiatomic CoFeNi complex concentrated alloy, Scr. Mater., 187 (2020) 30–36.
18. P. Li, A. Wang, C.T. Liu, A ductile high entropy alloy with attractive magnetic properties. J. Alloys Compd. **694**, 55–60 (2017)
19. P. Li, A. Wang, C.T. Liu, Composition dependence of structure, physical and mechanical properties of $FeCoNi(MnAl)_x$ high entropy alloys. Intermetallics **87**, 21–26 (2017)
20. T.T. Zuo, R.B. Li, X.J. Ren, Y. Zhang, Effects of Al and Si addition on the structure and properties of CoFeNi equal atomic ratio alloy. J. Magn. Magn. Mater. **371**, 60–68 (2014)
21. Y. Zhang, T. Zuo, Y. Cheng, P.K. Liaw, High-entropy alloys with high saturation magnetization, electrical resistivity, and malleability. Sci. Rep. **3**, 1455 (2013)
22. C. Zhao, J. Li, Y. He, J. Wang, W.Y. Wang, H. Kou, J. Wang, Effect of strong magnetic field on the microstructure and mechanical-magnetic properties of AlCoCrFeNi high-entropy alloy. J. Alloys Compd. **820**, 153407 (2020)
23. Y. Ma, Q. Wang, X. Zhou, J. Hao, B. Gault, Q. Zhang, C. Dong, T.-G. Nieh, A novel soft-magnetic B2-based multiprincipal-element alloy with a uniform distribution of coherent body-centered-cubic nanoprecipitates. Adv. Mater. **33**, 2006723 (2021)
24. L. Han, Z. Rao, I.R. SouzaFilho, F. Maccari, Y. Wei, G. Wu, A. Ahmadian, X. Zhou, O. Gutfleisch, D. Ponge, D. Raabe, Z. Li, Ultrastrong and ductile soft magnetic high-entropy alloys via coherent ordered nanoprecipitates. Adv. Mater. **33**, 2139 (2021)
25. Z. Rao, B. Dutta, F. Körmann, W. Lu, X. Zhou, C. Liu, A.K. da Silva, U. Wiedwald, M. Spasova, M. Farle, Beyond solid solution high-entropy alloys: tailoring magnetic properties via spinodal decomposition. Adv. Funct. Mater. **31**, 2007668 (2021)
26. Y. Zhang, M. Zhang, D. Li, T. Zuo, K. Zhou, M.C. Gao, B. Sun, T. Shen, Compositional design of soft magnetic high entropy alloys by minimizing magnetostriction coefficient in (Fe03Co05Ni02)100–x(Al1/3Si2/3)x system/. Metals **9**, 382 (2019)
27. C. Jung, K. Kang, A. Marshal, K.G. Pradeep, J.-B. Seol, H.M. Lee, P.-P. Choi, Effects of phase composition and elemental partitioning on soft magnetic properties of AlFeCoCrMn high entropy alloys. Acta Mater. **171**, 31–39 (2019)
28. G. Kresse, J. Hafner, Ab initio molecular dynamics for liquid metals. Phys. Rev. B **47**, 558 (1993)
29. G. Kresse, J. Furthmüller, Efficiency of ab-initio total energy calculations for metals and semiconductors using a plane-wave basis set. Comput. Mater. Sci. **6**, 15–50 (1996)
30. P.E. Blöchl, Projector augmented-wave method. Phys. Rev. B **50**, 17953 (1994)
31. J.P. Perdew, K. Burke, M. Ernzerhof, Generalized gradient approximation made simple. Phys. Rev. Lett. **77**, 3865 (1996)
32. A. Zunger, S.H. Wei, L.G. Ferreira, J.E. Bernard, Special quasirandom structures. Phys. Rev. Lett. **65**, 353–356 (1990)
33. A. Van De Walle, M. Asta, G. Ceder, The alloy theoretic automated toolkit: a user guide. Calphad **26**, 539–553 (2002)
34. A. Van de Walle, P. Tiwary, M. De Jong, D. Olmsted, M. Asta, A. Dick, D. Shin, Y. Wang, L.-Q. Chen, Z.-K. Liu, Efficient stochastic generation of special quasirandom structures. Calphad **42**, 13–18 (2013)
35. J.C.H. Spence, J. Taftø, ALCHEMI: a new technique for locating atoms in small crystals. J. Microsc. **130**, 147–154 (1983)
36. J.B. Nelson, D.P. Riley, An experimental investigation of extrapolation methods in the derivation of accurate unit-cell dimensions of crystals. Proc. Phys. Soc. **57**, 160 (1945)
37. I. Povstugar, P.-P. Choi, S. Neumeier, A. Bauer, C.H. Zenk, M. Göken, D. Raabe, Elemental partitioning and mechanical properties of Ti-and Ta-containing Co–Al–W-base superalloys studied by atom probe tomography and nanoindentation. Acta Mater. **78**, 78–85 (2014)
38. G. Herzer, Modern soft magnets: amorphous and nanocrystalline materials. Acta Mater. **61**, 718–734 (2013)
39. E.A. Stern, Rigid-band model of alloys. Phys. Rev. **157**, 544 (1967)
40. V.S. Bai, T. Rajasekharan, Evidence of a critical Mn-Mn distance for the onset of ferromagnetism in NiAs type compounds. J. Magn. Magn. Mater. **42**, 198–200 (1984)
41. J.C. Slater, Cohesion in monovalent metals. Phys. Rev. **35**, 509 (1930)
42. J.C. Slater, Atomic shielding constants. Phys. Rev. **36**, 57 (1930)
43. A. Sommerfeld, H. Bethe, Elektronentheorie der Metalle. Handbuch der Physik. XIV, in, Springer Heidelberg, 1956.
44. Q. Zeng, I. Baker, V. McCreary, Z. Yan, Soft ferromagnetism in nanostructured mechanical alloying FeCo-based powders. J. Magn. Magn. Mater. **318**, 28–38 (2007)
45. A.J. Albaaji, E.G. Castle, M.J. Reece, J.P. Hall, S.L. Evans, Enhancement in the elongation, yield strength and magnetic properties of

intermetallic FeCo alloy using spark plasma sintering. J. Mater. Sci. **52**, 13284–13295 (2017)
46. A.J. Albaaji, E.G. Castle, M.J. Reece, J.P. Hall, S.L. Evans, Influence of spark plasma sintering parameters on magnetic properties of FeCo alloy. AIP Adv. **8**, 047705 (2018)
47. A.I.C. Persiano, R.D. Rawlings, Effect of niobium additions on the structure and magnetic properties of equiatomic iron-cobalt alloys. J. Mater. Sci. **26**, 4026–4032 (1991)
48. K. Kawahara, M. Uehara, A possibility for developing high strength soft magnetic materials in FeCo-X alloys. J. Mater. Sci. **19**, 2575–2581 (1984)

Publisher's Note Springer Nature remains neutral with regard to jurisdictional claims in published maps and institutional affiliations.

Springer Nature or its licensor (e.g. a society or other partner) holds exclusive rights to this article under a publishing agreement with the author(s) or other rightsholder(s); author self-archiving of the accepted manuscript version of this article is solely governed by the terms of such publishing agreement and applicable law.